Check for updates

Online monitoring of lanthanide species with combined spectroscopy in flowing aqueous aerosol systems

Garrett LeCroy, [ID] †[a] Qiufeng Yang, [ID] †[a] Micah Raab,[b] Ruchi Gakhar [ID] *[a] and Ammon Williams [ID] *[b]

Combined spectroscopic analysis through absorption and laser-induced breakdown spectroscopy (LIBS) was used to monitor Nd and Pr concentrations in a flowing aqueous system. A unique, online sampling approach was employed that allowed for an approximately closed analysis loop of liquids from a reservoir. Absorption spectroscopy was performed with an optical flow cell, and LIBS was performed on an aerosol stream. Multivariate calibrations based on combined absorption and LIBS signals were built for Nd and Pr and then used to monitor concentrations in mixed solutions in a series of spiking tests. In these tests, the concentrations of Nd and Pr in solution were intermittently changed while spectroscopic signals were monitored in real-time. The combined spectroscopic signals and multivariate models were successful in monitoring changing concentrations of lanthanide species with high accuracy and minimal latency. Root-mean squared error of predictions were 0.015 mol L^{-1} and 0.019 mol L^{-1} for Nd and Pr respectively, and these lanthanides were able to be monitored to an accuracy of < 0.2 wt%. This work demonstrates both the capabilities of a sampling system for online analysis of liquids and the capabilities of multimodal spectroscopic characterization for real-time, continuous tracking of species in potentially hazardous liquid systems.

1 Introduction

Monitoring analytes in hazardous, difficult-to-access liquid flows is essential across various application spaces, including process control in industrial settings[1,2] and materials accountancy in the nuclear industry.[3,4] Indeed, the latter has strict regulatory requirements and international agreements that require adequate tracking of special nuclear materials in existing liquid reprocessing technologies[3,5,6] and pose a critical process-monitoring challenge for new Generation IV reactor concepts (*e.g.*, molten salt reactors)[7] or pyrochemical fuel reprocessing schemes.[8] Monitoring hazardous fluid flows presents significant challenges due to the harsh operating conditions of many industrial and nuclear applications that include high temperatures, corrosive environments, ionizing radiation, and chemical hazards. The need for process monitoring and real-time feedback is critical as changing compositions of fluid flows, such as the buildup of reaction products, corrosion products, and fission/decay products in nuclear

applications, can alter the chemistry of the liquid flows—resulting in safety and environmental hazards.[9] Sensors fall into two broad categories: (1) offline sensors, wherein fluid samples are collected and analyzed externally and (2) online/inline sensors, which directly probe fluid flows in real time. The distinction between online and inline is whether liquid is removed *via* a bypass for characterization (online) or not (inline).[10]

Offline quantitative analysis approaches such as inductively coupled plasma mass- or optical-emission spectrometry (ICP-MS/OES) and X-ray fluorescence (XRF) provide precise analyte concentration measurements (parts-per million or better) but involve relatively expensive and potentially hazardous physical sample collection, transfer, and preparation.[9,11] Additionally, offline techniques often involve considerable delays between sample collection and analysis, limiting their suitability for process monitoring requiring rapid feedback (*e.g.*, materials accountancy in nuclear reactors).

Online/inline analysis approaches involving optical spectroscopy are attractive due to the ability for remote analysis *via* fiber optic delivery/collection systems.[3,12] Common remote analysis techniques amenable to fiber optic systems include Raman spectroscopy,[13–15] absorption spectroscopy,[16,17] and laser induced breakdown spectroscopy (LIBS).[18,19] All of these spectroscopic techniques have varying advantages for different systems and can provide complementary information. For

[a]*Advanced Technology of Molten Salts, Idaho National Laboratory, Idaho Falls, Idaho 83415, USA. E-mail: ruchi.gakhar@inl.gov*

[b]*Material Minimization, Security & International Safeguards Department, Idaho National Laboratory, Idaho Falls, Idaho, 83415, USA. E-mail: ammon.williams@inl.gov*

† G. L. and Q. Y. contributed equally to this work.

example, Raman spectroscopy is powerful in the identification of molecular compounds but is not well-suited for analysis of metallic species or identification of oxidation states. Techniques such as LIBS however, provide elemental and even isotopic analysis, including of metallic species.[20,21] Furthermore, techniques like absorption spectroscopy can be used to readily determine species' oxidation states.[22] Combining spectroscopic characterization techniques can potentially build powerful monitoring capabilities.

Monitoring hazardous liquid flows with multiple spectroscopic characterization techniques has been used successfully across several examples. Schwantes *et al.* monitored Nd^{3+} concentrations in a nuclear fuel reprocessing liquid flow using absorption and Raman spectroscopy.[6] Lines *et al.* have demonstrated the ability to monitor nitrate and phosphate analytes in flowing aqueous systems from hazardous radiological waste also using absorption and Raman spectroscopy.[23] Koresaar *et al.* used LIBS and reflection/absorption spectroscopy to monitor mineral content in slurry samples.[16] This latter example shows that absorption spectroscopy and LIBS provide complements in combined elemental and oxidation state identification, though few other examples exist of these combined techniques in literature.

Electronic absorption spectroscopy probes analyte concentration and oxidation state, and, especially with the introduction of optical fiber-coupled light delivery and collection, allows for remote monitoring.[24] Indeed, absorption spectroscopy has been suggested and implemented for real-time materials monitoring in hazardous liquid flows since at least the 1950s where techniques were developed for online monitoring of uranium in aqueous processing streams,[25] and extensive work exists on monitoring hazardous liquid streams containing radiological hazards (*e.g.*, various oxidation states of uranium and plutonium) using absorption spectroscopy.[3,24,26–28]

LIBS provides elemental identification and offers useful features including sample pretreatment-free measurements, near real-time analysis, broad elemental coverage, and a typically low-parts-per million detection limit.[29,30] Additionally, LIBS can be performed on a variety of material matrices including solids, liquids, gases, and aerosols. LIBS makes use of a focused, pulsed laser source (typically nanosecond pulses) to generate high temperature plasma through dielectric breakdown on the material of interest. During the cooling process of the plasma, excited electrons transition to energetic ground states, generating discrete emission lines unique to a given element.[30] LIBS historically has limits of detection (LOD) an order of magnitude higher than those found from other analytical techniques like XRF.[31] However, LODs and predictive capabilities of LIBS have improved dramatically with the development of chemometric techniques that can deliver quantification results similar to ICP-MS analysis.[32]

LIBS is a semi-destructive technique where the local area of dielectric breakdown can be ablated, and this material ablation leads to crater formation in solids and splashing of material in liquid samples that increases shot-to-shot variations in plasma emission signal.[33,34] LIBS analysis of flowing aerosols can circumvent this issue and allow LIBS to be performed away from

the process fluid of interest (*e.g.*, LIBS delivery and collection optics can be remote to a hazardous stream). LIBS of aerosol streams has been used for detection of alkali and transition metals[35] and lanthanide species[18,36] with LODs of lanthanide species such as Gd and Ce down to approximately 200 ppm.

In the present work, we make use of combined online absorption and LIBS spectroscopic characterization to monitor two lanthanides (Nd and Pr) in an acidic aqueous process fluid. Though the process fluid in this work was an aqueous stream, the lanthanides chosen as analytes were selected because they represent two fission products present in molten salt reprocessing applications. Future work will focus on scaling insights from this current study to high-temperature molten salt applications, with the goal of developing an online sampling/monitoring mechanism for molten salt-based nuclear fuel reprocessing applications. Indeed, work on compositional analysis of LiCl–KCl eutectic salts in the Mark-IV electrorefiner (ER) at Idaho National Laboratory (INL) during reprocessing of sodium-bonded drive fuel from the Experimental Breeder Reactor II has shown that the lanthanide fission products Nd and Pr can be present in weight percents as high as 3 and 1 wt% respectively.[37]

While the analytes chosen for this work are intended to inform future work on molten salt systems, we do emphasize that a key aspect of this work was development of a mechanism to sample an arbitrary process fluid for online analysis.[38] This online sampling scheme can be applied to many different types of process fluids where the sampling mechanism allows for real-time spectroscopic measurements under near closed-loop conditions with minimal material loss. In this mechanism, absorption was measured in a flowing liquid cell (*i.e.*, a flow cell) and simultaneous LIBS was collected in an aerosol system. We demonstrate that the combination of the two techniques, alongside coupled multivariate modeling, provides the ability for real-time monitoring of aqueous fluid flows with changing composition. This work represents the first combined absorption and LIBS monitoring approach for lanthanide species in a flowing aqueous system and serves to demonstrate the capabilities of a unique mechanism for online sampling of a process fluid. Furthermore, this work demonstrates capabilities of combined spectroscopic approaches for real-time tracking of analytes that are relevant not only to liquid nuclear fuel reprocessing and molten salt reactor applications but to broader industrial hazardous liquid applications.

2 Methods

2.1 Materials and solution preparation

$NdCl_3$ (anhydrous, 99.99% trace metals basis) and $PrCl_3$ (anhydrous, 99.99% trace metals basis) were procured from Sigma-Aldrich and used without additional purification. A digital balance with an accuracy of 10^{-4} g was used to mass the salt. Aqueous solutions were prepared by dissolving $NdCl_3$ and/or $PrCl_3$ into 2% (v/v) nitric acid (HNO_3) in deionized (DI) water. The solutions were allowed to stir at room temperature for 30 min. Solution concentrations were measured with inductively coupled plasma mass spectrometry (ICP-MS) with an

Agilent 7900 instrument. Solutions were freshly prepared for each test to avoid possible contamination during storage.

2.2 Experimental setup for spectroscopic monitoring

Simultaneous absorption spectroscopy and LIBS were performed using a custom-built liquid recirculating system shown in Fig. 1.[38] A venturi pump ("venturi 1" in Fig. 1) supplied with argon gas created a vacuum that drew liquid from the process fluid reservoir through an optical flow cell where absorption spectroscopy was measured. After fluid passed through the optical flow cell, the liquid was mixed with argon gas from the venturi pump and partially aerosolized before being transported into a Collison nebulizer reservoir. The Collison nebulizer produced small liquid particles that were then transported *via* argon gas to an optical cell for LIBS data collection and finally to a coalescing filter for aerosol collection. Liquid in the Collison nebulizer reservoir was transported back to the primary process fluid reservoir *via* a second argon-supplied venturi pump ("venturi 2" in Fig. 1) such that the liquid level in the process fluid reservoir remained approximately constant. The argon pressure of the nebulizer was set at 40 pounds per square inch gauge (psig), and the argon pressure of the first venturi pump ("venturi 1") was set at 75 psig. The flow rate through this venturi pump was controlled with a needle valve at ≈ 4.5 L h^{-1}. The argon pressure through the second venturi pump that returned fluid from the nebulizer to the process liquid reservoir ("venturi 2") was set at 25 psig.

LIBS data collection was performed in a custom-built optical cell where aerosol was directed into the cell *via* an aerosol nozzle (Fig. 1).[38] The optical windows/components of the cell were maintained clean and free of aerosol deposition by using an argon sheath gas flow (gas flow rate was set at ≈ 22.6 L min^{-1}) that surrounded the flowing aerosol as used by Park *et al.* and Tjärnhage *et al.* in LIBS measurements of aerosol streams.[39,40]

2.3 Absorption spectroscopy

Absorption spectra were measured using a Cary 60 spectrophotometer, equipped with a xenon lamp covering a wavelength (λ) range of $\lambda = 190–1100$ nm. Absorption measurements were performed in transmission mode using a 5 mm pathlength flow cell (Avantes in-line stainless steel flow cell with SMA-905 connectors, $\lambda = 200–2500$ nm range). Absorption was reported as decadic absorbance (Abs$_{10}$) based on transmission (T) measurements where Abs$_{10} = -\log_{10}(T)$. Light was delivered to samples and collected *via* fiber optics (Fiberguide Industries Inc, core diameter 400 μm, NA = 0.22). Fiber optics were interfaced with the spectrophotometer through a fiber optic coupler from Harrick Scientific. The wavelength scale of the spectrophotometer over the range of 280–880 nm was verified and calibrated using a NIST certified reference material consisting of an aqueous solution of didymium perchlorate that was permanently sealed by heat fusion in a high-quality UV quartz cell (Starna Scientific). The flow cell was cleaned with DI water and 2% (v/v) HNO$_3$ solution before each sample run. Spectra were analyzed using Spectragryph software (version 1.2.11).[41] Spikes caused by grating/source changeovers of less than 7 nm in width were first removed from the spectra, then a Savitzky–Golay smoothing algorithm was applied using an interval of 8 nm and a fifth order polynomial function. An adaptive baseline was applied to each spectrum, with the coarseness of the baseline adjusted to optimize the fit while ensuring that no peaks were artificially diminished in intensity.

2.4 Laser-induced breakdown spectroscopy

Plasma for LIBS data collection was created using the output of a Q-Smart 450 Nd:YAG laser (Quantel USA) operating at a wavelength output of $\lambda = 1064$ nm, a shot energy of 40 mJ per shot, and a shot frequency of 4 Hz. The laser output was focused on the aerosol stream using a 75 mm focal length lens. Plasma
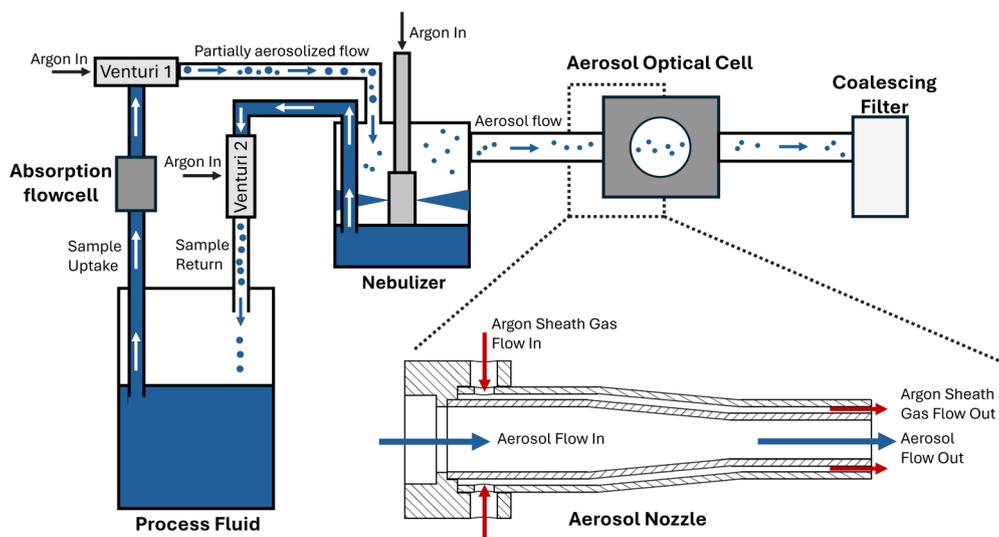

Fig. 1 Schematic overview of the liquid recirculating system used for spectroscopic characterization of aqueous process fluids in this work.[38] Fluid flows are shown with arrows. Zoomed-in regions shows aerosol flow directed by a nozzle into the optical cell.

emission was collected with an echelle spectrometer (Catalina Scientific EMU 120/65) equipped with an electron-multiplying charge-coupling device (EMCCD). Each spectrum was acquired using a gate delay of 3 μs and a gate width of 1 ms. Each spectrum was collected over a wavelength range of $\lambda =$ 350–950 nm and represents the average of 10 repetitions of 100 individual laser shots per repetition. All LIBS spectra were normalized by the intensity of the hydrogen emission line at $\lambda =$ 656.30 nm.

2.5 Sampling procedure

In this study, two types of measurements were obtained: constant-concentration circulation tests and circulation tests with intermittent sample spiking (*i.e.*, "spiking" tests).

2.5.1 Constant–concentration tests. Tests were performed using constant analyte concentrations to obtain spectroscopic calibration curves. The concentrations of solutions for calibration are given in Table 1, with values found by ICP-MS analysis. In these tests, ≈30 mL of each sample were prepared and circulated through the recirculating system with simultaneous absorption and LIBS measurements being performed. Following each test, a small aliquot of the solution was analyzed *via* ICP-MS to measure the solution composition.

2.5.2 Spiking tests. For the intermittent sample spiking tests, the initial process fluid was 2% (v/v) HNO_3 in water, and the fluid was spiked nine times by introducing samples with

different concentrations of aqueous $NdCl_3$ and $PrCl_3$ into the process fluid reservoir. Spike additions are shown in Table 2. Absorption and LIBS emission were continuously monitored for 100 minutes during the spiking tests. Absorption spectra were collected approximately every 1.2 minutes while LIBS spectra were collected every 0.5 minutes. The supplemental methods (see Section S1) describe the time-synchronization procedure used to link absorption data with LIBS data for regression analysis. Absorption spectra were used to monitor solution homogeneity in the system, and when at least three absorption spectra were collected with negligible changes (less than 1% change in peak absorbance), 5 mL of solution was sampled for ICP-MS analysis to verify the composition offline. See Fig. S1 for the resulting steady-state absorption spectra. The resulting steady-state solution concentrations are shown in Table 2 along with the relevant spike addition.

2.6 Calibration regression analysis

All regression was performed using open-source packages from the Python Scikit-Learn library.[42] Regression was performed using the calibration samples in Table 1 as the training data set, and the spiking samples shown in Table 2 as a set of independent, external validation samples. Univariate and multivariate regression in the form of multiple linear regression was used to predict Pr and Nd concentrations based on LIBS and absorbance spectroscopy data. For multivariate regression of absorption spectroscopy data, the peak absorbance of four absorption peaks, 443 nm and 467 nm for Pr^{3+}, and 741 nm and 865 nm for Nd^{3+}, were selected because they were the strongest absorbing peaks for each species that exhibited no spectral overlap. The Nd^{3+} absorbance peak at $\lambda = 795$ nm was not used for further analysis as this peak sat close to the region of spectrophotometer grating changeover and was prone to potential spikes in data resulting from the grating changeover. For multivariate regression of LIBS data, the intensities of six emission peaks in total (three each for Pr and Nd) were used for calibration: for Pr, emission peaks at $\lambda = 410.06$ nm, 511.08 nm, and 522.02 nm were used, and for Nd, emission peaks at $\lambda =$ 406.10 nm, 513.06 nm, and 531.97 nm were used. These peaks were selected as features with signal-to-background ratios (SBRs) with SBR > 2 and R^2 values of univariate calibration fits to

Table 1 Calibration sample compositions and labels

Sample ID	$NdCl_3$ [mol L^{-1}]	$PrCl_3$ [mol L^{-1}]
1	0.053	0
2	0.104	0
3	0.175	0
4	0.204	0
5	0	0.169
6	0	0.348
7	0	0.442
8	0	0.479
9	0.103	0.416
10	0.049	0.519
11	0.197	0.196
12	0.146	0.293

Table 2 Spiking test additions and resulting validation sample concentrations

Sample ID	Added sample	Volume [mL]	Steady state concentration[a] [mol L^{-1}] Nd/Pr
Baseline	2% v/v HNO_3	30	—/—
Spike 1	0.6 mol L^{-1} $NdCl_3$	5	0.132/—
Spike 2	1.6 mol L^{-1} $PrCl_3$	10	0.113/0.612
Spike 3	0.6 mol L^{-1} $NdCl_3$	10	0.288/0.483
Spike 4	2% v/v HNO_3	10	0.225/0.376
Spike 5	0.6 mol L^{-1} $NdCl_3$	10	0.353/0.306
Spike 6	1.6 mol L^{-1} $PrCl_3$	5	0.342/0.544
Spike 7	2% v/v HNO_3	5	0.324/0.509
Spike 8	1.6 mol L^{-1} $PrCl_3$	15	0.243/0.909
Spike 9	2% v/v HNO_3	40	0.126/0.469

[a] This concentration was found from offline ICP-MS analysis from samples collected after the process fluid composition homogenized.

the samples in Table 1 greater than 0.9. This criteria was satisfied by more than three LIBS emission peaks, so the three chosen were the emission peaks with the highest R^2 values of univariate calibration fits. Increasing the number of LIBS emission peaks included in the multivariate model beyond three per species did not lead to model improvements in this work.

Additionally, multivariate regression was performed on combined LIBS and absorption spectroscopy data ("combined model" in this work). For the combined multivariate regression, six LIBS emission peaks were used at $\lambda = 410.06$ nm, 511.08 nm, and 522.02 nm, 406.10 nm, 513.06 nm, and 531.97 nm, and four absorption peaks were used at $\lambda = 443$ nm, 467 nm, 741 nm and 865 nm. The dimension of the absorbance data was reduced by taking the sum of the peak absorbance for the 443 nm and 467 nm peaks to yield a single absorbance value representative of Pr^{3+} concentration, and similarly the sum of the 741 nm and 865 nm peak absorbances was used to yield a single absorbance value representative of Nd^{3+} concentration. This procedure of adding peak absorbance prior to any additional preprocessing steps prevented (1) overfitting of data in multilinear regression and (2) provided better predictive capabilities in this work, though this procedure did not generally improve predictions when applied to LIBS emission peaks.

Prior to performing multivariate regression analysis, absorbance and LIBS emission peaks (after normalization by the H emission line) were further preprocessed using Min–Max scaling in the Scikit-Learn library,[42] such that all feature intensities fell between values of 0–1 arbitrary units.

3 Results and discussion

3.1 Spectroscopic data at constant concentrations

3.1.1 Absorbance spectroscopy. Univariate calibration curves for Pr^{3+} and Nd^{3+} in aqueous solution were first developed based on absorption spectroscopy and LIBS results using the twelve calibration samples shown in Table 1. Absorption spectroscopy was used to monitor the electronic absorption spectra of Pr^{3+} and Nd^{3+} in aqueous solution based on the Beer–Lambert Law ($Abs_{10} \propto c$, where c is the analyte concentration). In this work, absorbance of a given transition is defined as the Abs_{10} value at the wavelength of maximum absorbance (λ_{max}) for a given electronic transition band.

The electronic absorption spectrum of Nd^{3+} ($^4I_{9/2}$ ground state) is shown in Fig. 2a and the spectrum of Pr^{3+} ($^3H_4$ ground state) is shown in Fig. 2b, with absorption peaks labeled by excited state term symbols.[22,43] A mixed sample comprising a mixture of 0.146 mol L^{-1} Nd^{3+} and 0.293 mol L^{-1} Pr^{3+} (sample 12, Table 1) is shown in Fig. 2c, demonstrating that the electronic absorption peaks of Pr^{3+} and Nd^{3+} do not overlap, except for the region between $\lambda = 575$–600 nm. Univariate calibration curves based on the peak absorbance of various absorbance bands for both Nd^{3+} and Pr^{3+} are shown in Fig. 3. The R^2 values of linear regression fits are provided in Table 3, along with limits of detection (LOD) as determined by eqn (1).
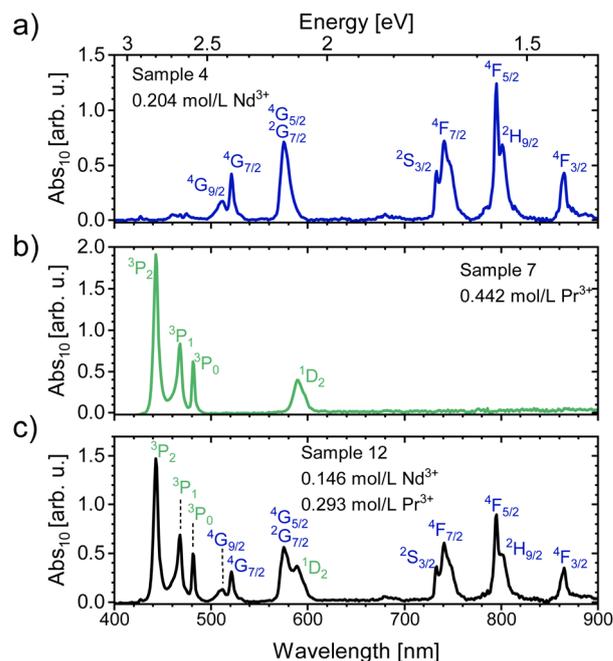

Fig. 2 Electronic absorption spectra for (a) sample ID 4 (Table 1) with 0.204 mol L^{-1} Nd^{3+}, (b) sample ID 7 (Table 1) with 0.442 mol L^{-1} Pr^{3+}, and (c) sample ID 12 (Table 1) with mixed 0.146 mol L^{-1} Nd^{3+} and 0.293 mol L^{-1} Pr^{3+}. The excited state term symbols represent transitions from the $^4I_{9/2}$ ground state of Nd^{3+} and the $^3H_4$ ground state of Pr^{3+}.[22,43]
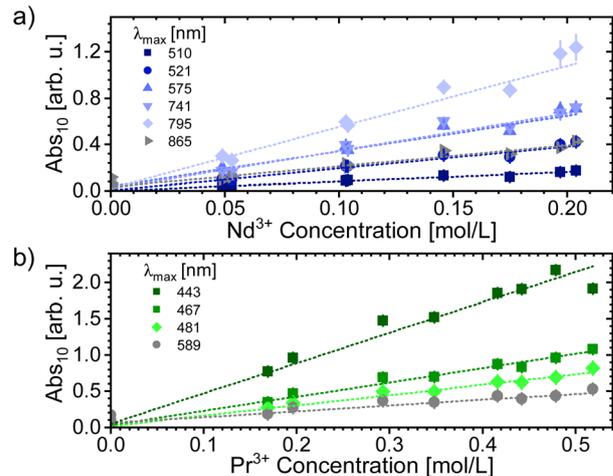

Fig. 3 Univariate calibration curves of absorption spectroscopy for (a) Nd^{3+} and (b) Pr^{3+} based on the samples shown in Table 1. Data points represent the average of 3–6 individual absorption measurements (unnormalized), and error bars represent the standard deviation of the measurements. Error bars are below the symbol point size in panel (b).

$$\text{LOD} = \frac{3\sigma}{m} \qquad (1)$$

where m is the slope of the linear regression fit and σ is the standard deviation of the measured signal from blank samples (samples with either no Nd^{3+} or Pr^{3+}, see Table 1). The

Table 3 R^2 and LOD for univariate absorption spectroscopy calibrations

	Nd^{3+}				Pr^{3+}				
Band λ_{max} [nm]	795	575	741	521	510	443	467	481	589
R^2	0.980	0.982	0.973	0.980	0.956	0.987	0.995	0.998	0.990
LOD [mol L^{-1}]	0.008	0.008	0.006	0.006	0.017	0.009	0.022	0.033	0.042

absorbance across multiple bands exhibit linear behavior ($R^2 > 0.95$) with respect to analyte concentration (Fig. 3). The LOD varies among the absorption bands used for univariate calibration, though LOD is generally lower for all Nd^{3+} univariate calibration curves than Pr^{3+} (Table 3). The univariate calibration curve for the $\lambda_{max} = 443$ nm band yields the lowest LOD for Pr^{3+} with a limit of 0.009 mol L^{-1}, while the calibration curves for the $\lambda_{max} = 521$ nm and 741 nm yield the lowest LOD for Nd^{3+} with limits of 0.006 mol L^{-1}.

3.1.2 LIBS. Simultaneous to absorption spectroscopy data collection on the liquid stream, LIBS was collected on the aerosol stream (see Fig. 1). A representative sample of LIBS data is shown in Fig. 4 for sample 12 (Table 1) comprising a mixture of Nd^{3+} and Pr^{3+}. Additional LIBS emission peaks of this sample are shown in Fig. S2 of the supplemental. Lines from argon (Ar), praseodymium (Pr), neodymium (Nd), hydrogen (H), and oxygen (O) were identified and verified using the NIST atomic spectra database,[44] with representative lines highlighted in Fig. 4. Argon emission lines were strongest, as argon served as the carrying gas for the aerosol. Five emission wavelengths (λ_{emiss}) were selected for both Nd and Pr for univariate calibration, shown in Fig. 5.

The peak intensities of LIBS spectra were normalized by the intensity of the $\lambda_{emiss} = 656.30$ nm H emission line, as described in the Methods section. Corresponding R^2 values of linear regression fits and LODs are shown in Table 4. While emission intensity was linear with analyte concentration ($R^2 > 0.90$), the R^2 values for univariate calibration of LIBS emission data are lower than those reported in Table 3 for univariate calibrations of absorption data. Consequently, the LOD values are higher by
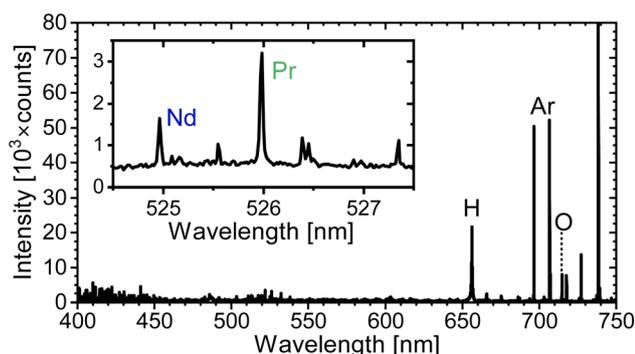
a factor of $\approx 2\times$ in LIBS calibration data compared to absorption calibration data, with the lowest LOD value of 0.020 mol L^{-1} for Pr and 0.012 mol L^{-1} for Nd. The generally worse performance of univariate LIBS calibrations compared to absorbance calibrations is thought to be a feature of either inherent shot-to-shot variation in LIBS of aerosolized liquid droplets,[45] or is a feature of slight variations in nebulizer and/or sheath-gas flow (Fig. 1) that results in variations of the aerosol stream across samples. There is also the possibility that evaporation of water in the aerosol stream due to the dry argon-gas flow results in variations in the H emission line that was used for sample normalization.

3.2 Validation of univariate calibrations and multivariate calibrations

To assess the sensitivity of spectroscopic characterization in the recirculating system design depicted in Fig. 1, a series of "spiking" tests were performed as described in the Methods section, wherein additions of either Pr^{3+}, Nd^{3+}, or blank (2% v/v HNO$_3$) solution to the process vessel were made while real-time absorption and LIBS spectroscopic characterization was performed. The additions and corresponding sample labels are shown in Table 2. The entire process fluid was allowed to homogenize (see Methods section) prior to conducting the next spike. This testing allowed the spiking tests to yield a set of
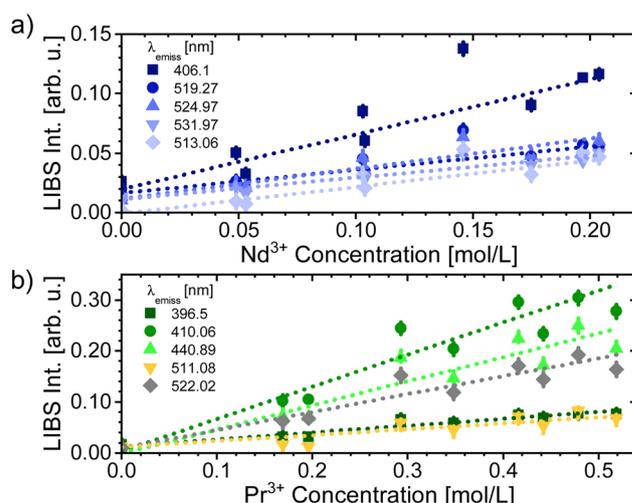

Fig. 4 LIBS spectrum for sample ID 12 (Table 1) with mixed 0.146 mol L^{-1} Nd^{3+} and 0.293 mol L^{-1} Pr^{3+}. Representative peaks for H, Ar, O, Nd, and Pr are labeled. The inset highlights the Nd emission peak at 524.96 nm and the Pr emission peak at 525.98 nm. Other minor emission peaks from Nd and Pr are seen in the inset. More emission peaks are shown in Fig. S1.

Fig. 5 Univariate calibration curves as measured by LIBS emission (a) Nd and (b) Pr based on the samples shown in Table 1. Data points represent the average of 10 individual LIBS measurements normalized by the $\lambda = 656.30$ nm H emission line, and error bars represent the standard deviation of the measurements.

Table 4 R^2 and LOD for univariate LIBS spectroscopy calibrations

	Nd					Pr				
Band λ_{emiss} [nm]	406.1	519.27	524.97	531.97	513.06	396.5	410.06	440.89	511.08	522.02
R^2	0.920	0.903	0.928	0.944	0.930	0.951	0.977	0.970	0.974	0.971
LOD [mol L^{-1}]	0.017	0.015	0.012	0.023	0.015	0.021	0.024	0.025	0.025	0.020

validation samples for the calibration curves based on either absorption spectroscopy (Fig. 3) or LIBS (Fig. 5). These validation samples, including spike label and resulting solution concentrations of analytes measured by ICP-MS analysis, are shown in Table 2. We emphasize that this set of validation samples was not used in the training data set, and acts as an independent, external validation to the model predictions.

Fig. 6a and b show the performance of representative univariate calibrations for either absorption spectroscopy or LIBS in predicting analyte concentration of the validation spike test samples. Model performance was evaluated using two metrics: the root-mean squared error of prediction (RMSEP) and the root-mean squared error of cross validation (RMSECV), both defined by eqn (2).

$$\text{RMSE}(P)(\text{CV}) = \left(\frac{\sum \left(y_{\text{pred}}^i - y_{\text{valid,ICP-MS}}^i \right)^2}{N} \right)^{1/2} \quad (2)$$

where y_{pred}^i represents the model prediction of the ith sample of the validation test set (Table 2) as based on either LIBS or

absorption spectroscopic signals from that sample for RMSEP or y_{pred}^i presents the model prediction as based on the cross-validation of the training test set (Table 1) for RMSECV calculations, $y_{\text{valid,ICP-MS}}^i$ represents the known concentration of the ith sample of the validation set for RMSEP or the training set for RMSECV as found by ICP-MS analysis, and N represents the number of samples in the validation set ($N = 9$ for RMSEP and $N = 12$ for RMSECV in this work). RMSEP measures errors in model predictions of concentrations on an independent validation sample set, which, in this case, were the spiking test samples (Table 2). Cross-validation for RMSECV was determined using a leave-one out cross-validation (LOOCV), where each sample from the training set (Table 1) was excluded from the model training set one sample at a time and then analyzed against the model predictions based on all other training samples.

For the univariate calibrations of Nd^{3+}, the absorption band centered at $\lambda = 741$ nm and the LIBS emission line at $\lambda = 531.97$ exhibited the lowest RMSEP, and these are the representative samples shown in Fig. 6a and b. For Pr^{3+}, the absorption band at $\lambda = 467$ nm and the LIBS emission line at $\lambda = 410.06$ nm displayed the lowest RMSEP for their respective measurements and are shown in Fig. 6a and b. The prediction R^2 values and RMSEP/RMSECV values for the univariate calibrations of both Nd and Pr, as shown in Fig. 6a and b, are listed in Table 5.

Predictive capabilities, as indicated by lower RMSEP/RMSECV values, were enhanced marginally using multivariate regression. The prediction R^2 and RMSEP/RMSECV values for the multivariate calibrations shown in Fig. 6c and d are given in Table 5. For all prediction models, Table 5 shows that the RMSEP and RMSECV values are similar (within $\approx 1.5\times$), except for the univariate prediction of Pr concentration based on absorption spectroscopy, which shows an RMSEP value more than twice the RMSECV value. This result is possibly related to the validation concentration range maximum being larger than the training concentration range, though this does not appear to generally affect other model predictions. The results in Table 5 suggest that the models of this work, when trained with the training data set of Table 1 and then applied to the external validation sample set of Table 2, provide reasonable predictive capabilities. Additionally, similarities in RMSEP/RMSECV generally suggest that the models developed are (1) not especially sensitive to changes in the calibration data set and (2) not overfit with an excessive number of multivariate parameters.

Multivariate calibrations generally also led to predictions that lay closer to the parity line (dashed line) shown in Fig. 6 than the univariate calibrations. This manifests as RMSEP/RMSECV values for both Nd and Pr predictions being lower using multivariate predictions. The only exception was the
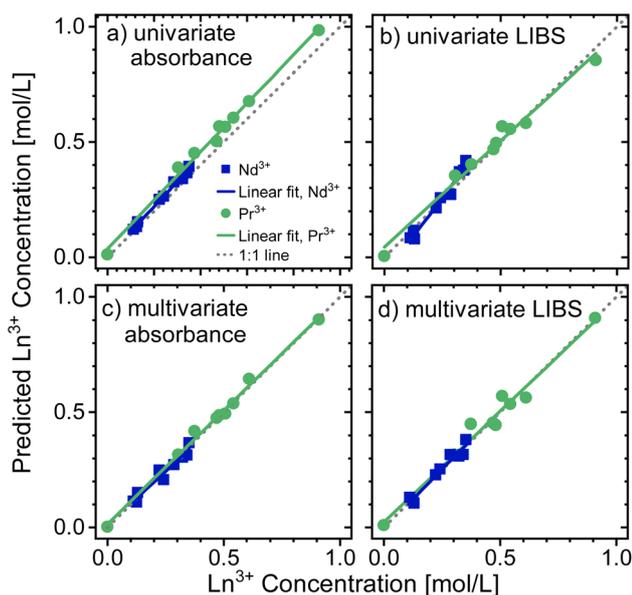

Fig. 6 Performance of univariate and multivariate calibration curves based on the training calibration sample set (Table 1) on predicting spike–testing validation sample compositions (Table 2). The performance of the (a) univariate absorption spectroscopy calibrations using the absorption band centered at $\lambda = 467$ nm for Pr^{3+} and the band centered at $\lambda = 741$ nm for Nd^{3+} and (b) LIBS univariate calibrations using the 410.06 nm emission line for Pr and the 531.97 nm emission line for Nd. The performance of the (c) absorption spectroscopy multivariate calibrations and (d) LIBS multivariate calibrations.

Table 5 Prediction statistics for univariate and multivariate calibrations

Model label		Nd		Pr	
		$R^{2\ a}$	RMSECV/RMSEP [mol L^{-1}]	$R^{2\ a}$	RMSECV/RMSEP [mol L^{-1}]
Absorption	Univariate[b]	0.996	0.013/0.021	0.997	0.021/0.055
	Multivariate	0.994	0.016/0.023	0.996	0.015/0.021
LIBS	Univariate[c]	0.987	0.031/0.031	0.977	0.042/0.034
	Multivariate	0.978	0.025/0.020	0.986	0.031/0.028
Combined	Multivariate	0.995	0.011/0.015	0.997	0.013/0.019

[a] R^2 of linear regression fits to the parity plots (solids lines shown in Fig. 6 and 7). [b] Univariate predictions based on absorption spectroscopy are shown for the bands centered at $\lambda = 741$ nm for Nd^{3+} and at $\lambda = 467$ nm for Pr^{3+}. [c] Univariate predictions based on LIBS are shown for the emission lines centered at $\lambda = 531.97$ nm for Nd and $\lambda = 410.06$ nm for Pr.

multivariate prediction of Nd concentration based on absorption spectroscopy. RMSEP/RMSECV values were also generally lower in predictions (both univariate and multivariate) based on absorption data than values based on predictions from LIBS data. This discrepancy possibly arises from shot-to-shot variation in LIBS data that persists despite the normalization procedure applied in this work.

A key advantage of multivariate predictions though is the ability to integrate the measurements from both absorption spectroscopy and LIBS into a single, unified model, referred to as the "combined" model in this work (see Methods section). To achieve this, peak absorbance from four absorption bands was summed into two values representative of Pr and Nd concentrations, and the LIBS emission intensity from six emission bands (three emission bands each for Nd and Pr) as used in the multivariate LIBS data, were combined into a single multiple linear regression model. The results of this combined model in predicting spike testing validation sample compositions are shown in Fig. 7, with the resulting R^2 of linear regression fits to the predicted data and RMSEP/RMSECV values provided in Table 5. For Nd, the RMSEP value is 0.015 mol L^{-1} and the RMSEP value is 0.019 mol L^{-1} for Pr. These RMSEP values indicate the combined model performs well in predicting validation set concentrations outside of the initial training range of concentrations (see vertical lines in Fig. 7). Though the predictive capabilities of the combined model are only marginally better than those of multivariate absorbance data, predictive capabilities are nonetheless improved for both Nd^{3+} and Pr^{3+} species in this work, and we argue that this work adds to the growing body of literature on using combined spectroscopic techniques for process monitoring.[13]

3.3 Real-time monitoring of spike tests using combined spectroscopy approaches

Model predictions of analyte concentration are valuable in their ability to monitor processes in a real-time fashion. Using absorption and LIBS spectroscopic signals collected during fluid spike-testing, the combined multivariate regression model of this work was used to predict Nd and Pr concentrations in the process fluid in real-time. The monitoring capabilities of separate multivariate models based on absorption spectroscopy (Fig. 6c) or LIBS (Fig. 6d) individually are shown in Fig. S4, and it

is shown that the analyte composition predictions of either data set alone are comparable, justifying the use of the combined model (see Fig. S5 for additional comparison of the placement of absorption and LIBS signal collection). The combined model predictions for both Nd and Pr concentrations as functions of time are shown by solid lines in Fig. 8. The time points of spike fluid addition and resulting concentrations measured by ICP-MS measurements are highlighted. Qualitatively, the model predictions align with the expected changes in analyte concentration during the nine spikes performed. For instance, the addition of spike 2 (10 mL of 1.6 mol L^{-1} PrCl$_3$) leads to a rapid increase in the model predictions of Pr concentration within less than 3 minutes. Similarly, the dilution of the process fluid by 40 mL of 2% HNO$_3$ at spike 9 results in a rapid decrease in model predictions of both Pr and Nd concentrations as would be expected from process fluid dilution. A single point with
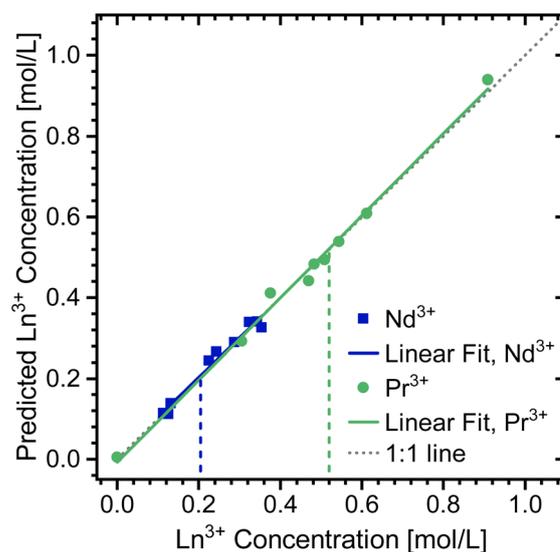

Fig. 7 Performance of multivariate calibration curves based on the training calibration sample set (Table 1) on predicting spike-testing validation sample composition (Table 2) using a combined multiple linear regression model with both absorption spectroscopy and LIBS emission data. Solid lines show linear regression fits to the predicted data, and the dashed line shows a line of slope 1. Vertical, dashed lines identify the maximum concentration used in the training data set (Table 1).
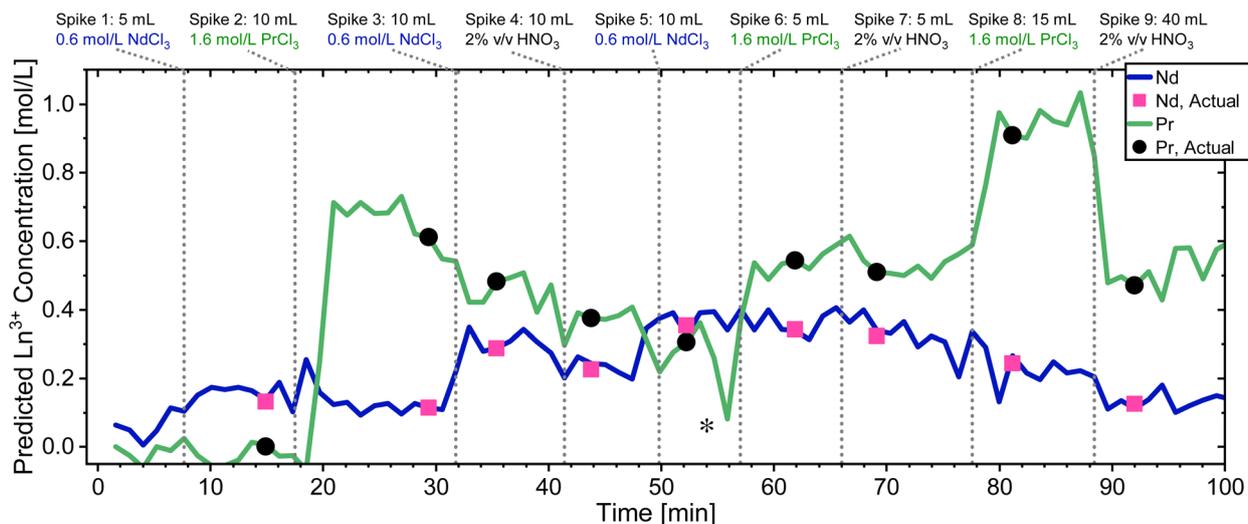
Fig. 8 Performance of combined multivariate calibrations (sample training set from Table 1) on predicting analyte concentration during real-time monitoring of spectroscopic signals during spike testing. The predicted Nd and Pr concentrations (blue and green lines) are based on the experimental spectroscopic signals from absorption spectroscopy and LIBS coupled with the combined multivariate model. Time of spike additions and quantity/analyte added are shown with vertical, dashed lines. The pink squares and black dots show points where samples were taken for ICP-MS and the resulting Nd and Pr concentrations, respectively. A single point of anomalously low predicted Pr value is highlighted with an asterisk (*). Fig. S3 shows details on expected issue at this point.

anomalously low predicted Pr values is highlighted in Fig. 8, and it is suspected that mild variations in fluid flow through the recirculating system (*e.g.*, bubble uptake through absorption flow cell in Fig. 1) could result in sudden spectroscopic signal deviations. Likely, the absorption flowcell is particularly susceptible to these signal deviations. Fig. S3 shows the raw absorbance data collected around the time of the anomalous point in Fig. 8 and a sudden deviation in signal can be seen. A highly simplified model of fluid flows in the sampling mechanism of Fig. 1 (see discussion around Fig. S5) provides some intuition on why absorbance measurements may be more susceptible to sudden flow disturbances than LIBS. Briefly, the aerosol nebulizer acts to average fluid compositions over a short time period; whereas the absorption flow cell, positioned close to the fluid uptake of the process fluid reservoir, responds rapidly to sudden changes in that fluid uptake. Despite this single anomalous predicted point, the model's predictive capabilities are quantitatively robust, as highlighted by the similarity of model predictions to concentrations determined by ICP-MS (black circles and pink squares for Pr and Nd, respectively in Fig. 8) and also indicated by low RMSEP values in the spike testing validation data (shown in Table 5).

The combined model effectively tracks the expected changes in analyte concentration with spike addition. Using RMSECV as an approximation of uncertainty in model predictions,[46] the uncertainty in materials tracking accountancy during the spike-testing period can be estimated. Nd concentrations ranged from 0.113 mol L^{-1} to 0.353 mol L^{-1} (1.63 to 5.09 wt%), and Pr concentrations ranged from 0.306 mol L^{-1} to 0.909 mol L^{-1} (4.31 to 12.81 wt%). The resulting RMSECV values from the combined multivariate predictions yield relative errors of 0.159 wt% for Nd and 0.183 wt% for Pr. Though this work was performed on an aqueous process stream, this current study is meant to inform future work on process monitoring in molten salt nuclear applications where lanthanide fission products are important components.[37] Using compositional analysis from Mark IV ER salts at INL[37] that found Nd presence in eutectic LiCl–KCl from ≈ 1–3 wt% and Pr from ≈ 0.3–1 wt% shows that the relative monitoring errors found in this work for Nd (0.159 wt%) could potentially be sufficient for Nd monitoring in pyroprocessing applications. However, monitoring Pr concentrations in this application would likely require lower relative wt% errors due to the generally smaller presence of Pr, and future work will need to consider this requirement when scaling the sampling scheme and spectroscopic analysis of this work to molten salt applications.

4 Conclusions

Spectroscopic monitoring offers the potential for remote, real-time analysis of hazardous liquid compositions in industrial processes and nuclear aqueous reprocessing applications. This work demonstrates a unique, online sampling system that allows near-simultaneous absorption and LIBS spectroscopic measurements on lanthanide species in aqueous fluid flows. Critically, this sampling system could be easily integrated into a wide variety of potential process fluids. Nd^{3+} and Pr^{3+} were used as surrogate species for potential fission products in aqueous reprocessing streams. The combination of absorption and LIBS allows for complementary analysis by monitoring features such as analyte oxidation state and elemental composition. Combined spectroscopic signals were used to build multivariate models for prediction of mixed Nd or Pr concentrations in aqueous solutions. These models showed good

predictive capabilities with an RMSEP value for Nd concentration prediction of 0.015 mol L^{-1} and a value for Pr concentration prediction of 0.019 mol L^{-1}. The predictive capabilities of the models were sufficient to provide real-time analyte monitoring in a series of spike tests where analyte concentrations in an aqueous process fluid were intermittently changed. Changes in solution composition predictions based on the multivariate models and combined spectroscopic signals displayed little time delay from the addition of analyte spikes. This demonstrates that the sampling technique and combined spectroscopic monitoring of this work are potentially feasible for real-time monitoring of hazardous liquid flows with changing compositions.

Author contributions

Conceptualization, methodology, A. W. and R. G.; Software, G. L., A. W and M. R.; investigation, resources, data curation, writing, Q. Y., G. L., A. W., R. G.; project administration and funding acquisition, A. W. and R. G. All authors have read and agreed to the published version of the manuscript.

Conflicts of interest

The authors have no conflicts to declare.

Data availability

All data shown in plots of the main text is available at https://doi.org/10.5281/zenodo.17154953.

Additional details on absorption and LIBS time-synchronization, steady-state absorbance spectra, and spike-test concentration monitoring using absorption and LIBS data individually. See DOI: https://doi.org/10.1039/d5ra04116c.

Acknowledgements

Notes and references

1 N. K. Rai and A. K. Rai, *J. Hazard. Mater.*, 2008, **150**, 835–838.
2 T. Karpate, K. M. Muhammed Shameem, R. Nayak, V. K. Unnikrishnan and C. Santhosh, LIBS: a potential tool for industrial/agricultural waste water analysis, *SPIE*, 2016, **9893**, 989317.
3 G. Boisde, F. Blanc and J.-J. Perez, *Talanta*, 1988, **35**, 75–82.
4 R. J. Lascola, P. E. O'Rourke, E. A. Kyser, D. M. Immel, J. R. Plummer and E. V. Evans, *Spectrophotometers for Plutonium Monitoring in HB-Line, Savannah River Site (SRS), Aiken, SC (United States) Report SRNL-STI-2015-00454*, 2016.
5 D. O. Kirsanov, V. Babain, M. Agafonova-Moroz, A. Lumpov and A. Legin, *Radiochim. Acta*, 2013, **101**, 149–154.
6 J. M. Schwantes, S. A. Bryan, C. R. Orton, T. G. Levitskaia, S. H. Pratt, C. G. Fraga and J. B. Coble, *Procedia Chem.*, 2012, **7**, 716–724.
7 K. K. Hogue, N. Luciano, M. Krupcale, R. Elzohery and L. G. Evans, *Planning for Material Control and Accountancy at Liquid Fueled Molten Salt Reactors Report ORNL/SPR-2023/3181; TRN: US2408047*, Oak Ridge National Laboratory (ORNL), Oak Ridge, TN (United States), 2024.
8 T.-S. Yoo and G. L. Fredrickson, *Engineering Scale Pyroprocessing Activities in the United States*, Idaho national laboratory report, 2023.
9 S. A. Bryan, T. G. Levitskaia, A. J. Casella, J. M. Peterson, A. M. Johnsen, A. M. Lines and E. M. Thomas, in *4 - Spectroscopic On-Line Monitoring for Process Control and Safeguarding of Radiochemical Streams in Nuclear Fuel Reprocessing Facilities*, ed. K. L. Nash and G. J. Lumetta, Woodhead Publishing, 2011, pp. 95–119.
10 N. Kroell, X. Chen, K. Greiff and A. Feil, *Waste Manage.*, 2022, **149**, 259–290.
11 D. Kirsanov, V. Babain, M. Agafonova-Moroz, A. Lumpov and A. Legin, *Radiochim. Acta*, 2012, **100**, 185–188.
12 P. Tse, S. A. Bryan, N. P. Bessen, A. M. Lines and J. C. Shafer, *Anal. Chim. Acta*, 2020, **1107**, 1–13.
13 A. M. Lines, G. B. Hall, S. Asmussen, J. Allred, S. Sinkov, F. Heller, N. Gallagher, G. J. Lumetta and S. A. Bryan, *ACS Sens.*, 2020, **5**, 2467–2475.
14 A. M. Lines, J. M. Bello, C. Gasbarro and S. A. Bryan, *Anal. Chem.*, 2022, **94**, 3652–3660.
15 G. J. Lumetta, J. C. Braley, J. M. Peterson, S. A. Bryan and T. G. Levitskaia, *Environ. Sci. Technol.*, 2012, **46**, 6190–6197.
16 N. Khajehzadeh, O. Haavisto and L. Koresaar, *Miner. Eng.*, 2017, **113**, 83–94.
17 L. H. Espinoza, D. Lucas and D. Littlejohn, *Appl. Spectrosc.*, 1999, **53**, 97–102.
18 H. B. Andrews and K. G. Myhre, *Appl. Spectrosc.*, 2022, **76**, 877–886.
19 A. Williams and S. Phongikaroon, *Appl. Spectrosc.*, 2017, **71**, 744–749.
20 C. Rinaldi, M. Pozzi, N. Boggio and J. Vorobioff, *Spectrochim. Acta, Part B*, 2020, **167**, 105841.
21 R. E. Russo, J. J. González, D. Oropeza, C. Liu, J. Chirinos and G. C. Y. Chan, *Spectrochim. Acta, Part B*, 2024, **216**, 106928.
22 W. T. Carnall, in *Chapter 24 the Absorption and Fluorescence Spectra of Rare Earth Ions in Solution*, Elsevier, 1979, vol. 3, pp. 171–208.
23 A. M. Lines, P. Tse, H. M. Felmy, J. M. Wilson, J. Shafer, K. M. Denslow, A. N. Still, C. King and S. A. Bryan, *Ind. Eng. Chem. Res.*, 2019, **58**, 21194–21200.
24 G. Boisde and J. J. Perez, *2nd Intl Conf on Optical Fiber Sensors*: OFS'84, 1984, pp. 227–232.
25 F. A. Scott and W. P. Van Meter, *The Design and Construction of an In-Line Photometer Sensing Unit, Hanford Atomic Products Operation Report HW-39926*, 1955.

26 D. T. Bostick, *Simultaneous Analysis of Uranium and Nitrate Report ORNL/TM-6292*, Oak Ridge National Lab. (ORNL), Oak Ridge, TN (United States), 1978.

27 J. Bürck, *Anal. Chim. Acta*, 1991, **254**, 159–165.

28 M. Kumar, S. Suman, S. Pugazhendi, K. Dhamodharan and K. A. Venkatesan, *Talanta*, 2024, **280**, 126673.

29 S. Guirado, F. J. Fortes, V. Lazic and J. J. Laserna, *Spectrochim. Acta, Part B*, 2012, **74–75**, 137–143.

30 D. A. Cremers and L. J. Radziemski, *Handbook of Laser-Induced Breakdown Spectroscopy*, John Wiley & Sons Ltd, 2013.

31 H. M. Solo-Gabriele, T. G. Townsend, D. W. Hahn, T. M. Moskal, N. Hosein, J. Jambeck and G. Jacobi, *Waste Manage.*, 2004, **24**, 413–424.

32 C. R. Bhatt, F. Y. Yueh and J. P. Singh, *Appl. Opt.*, 2017, **56**, 2280–2287.

33 G. Hull, H. Lambert, K. Haroon, P. Coffey, T. Kerry, E. D. McNaghten, C. A. Sharrad and P. Martin, *J. Anal. At. Spectrom.*, 2021, **36**, 92–102.

34 B. N. Chichkov, C. Momma, S. Nolte, F. von Alvensleben and A. Tünnermann, *Appl. Phys. A:Mater. Sci. Process.*, 1996, **63**, 109–115.

35 D. W. Hahn, J. E. Carranza, G. R. Arsenault, H. A. Johnsen and K. R. Hencken, *Rev. Sci. Instrum.*, 2001, **72**, 3706–3713.

36 A. N. Williams and S. Phongikaroon, *Appl. Spectrosc.*, 2016, **70**, 1700–1708.

37 T. Y. Karlsson, G. L. Fredrickson, T.-S. Yoo, D. Vaden, M. N. Patterson and V. Utgikar, *J. Nucl. Mater.*, 2019, **520**, 87–95.

38 A. Williams, R. Gakhar and P. Sabharwall, Battelle Energy Alliance LLC, Material management with continuous online high-temperature liquid sampling and analysis, *US pat.*, 18/612,061, 2024.

39 K. Park, G. Cho and J.-H. Kwak, *Aerosol Sci. Technol.*, 2009, **43**, 375–386.

40 T. Tjärnhage, P.-Å. Gradmark, A. Larsson, A. Mohammed, L. Landström, E. Sagerfors, P. Jonsson, F. Kullander and M. Andersson, *Opt. Commun.*, 2013, **296**, 106–108.

41 F. Menges, *Spectragryph - Optical Spectroscopy Software*, 2022, http://www.effemm2.de/spectragryph/.

42 F. Pedregosa, G. Varoquaux, A. Gramfort, V. Michel, B. Thirion, O. Grisel, M. Blondel, P. Prettenhofer, R. Weiss, V. Dubourg, J. Vanderplas, A. Passos, D. Cournapeau, M. Brucher, M. Perrot and E. Duchesnay, *J. Mach. Learn. Res.*, 2011, **12**, 2825–2830.

43 G. H. Dieke and H. M. Crosswhite, *Appl. Opt.*, 1963, **2**, 675–686.

44 A. Kramida, Y. Ralchenko, J. Reader and N. A. Team, *NIST Atomic Spectra Database*, 2025, https://www.physics.nist.gov/asd.

45 J. E. Carranza and D. W. Hahn, *J. Anal. At. Spectrom.*, 2002, **17**, 1534–1539.

46 N. M. Faber and R. Bro, *Chemom. Intell. Lab. Syst.*, 2002, **61**, 133–149.